

www.acsanm.org Article

GaAs/GaAsSb Core—Shell Configured Nanowire-Based Avalanche Photodiodes up to 1.3 μ m Light Detection

Rabin Pokharel, Hirandeep Kuchoor, Mehul Parakh, Shisir Devkota, Kendall Dawkins, Priyanka Ramaswamy, Jia Li, Christopher Winkler, Lew Reynolds, and S. Iyer*



Cite This: ACS Appl. Nano Mater. 2023, 6, 5093-5105



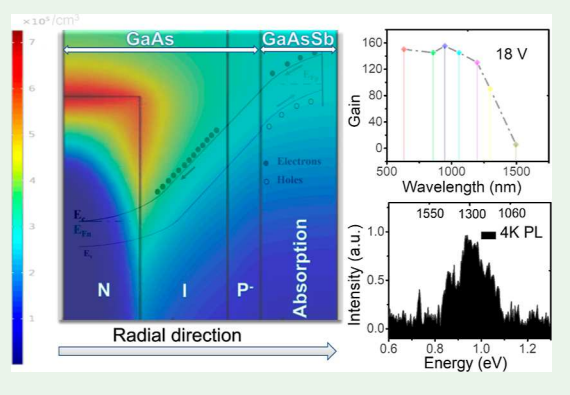
ACCESS I

III Metrics & More

Article Recommendations

Supporting Information

ABSTRACT: We report the first study on a GaAs/GaAsSb core—shell (CS)-configured nanowire (NW)-based separate absorption, charge control, and multiplication region avalanche photodiode (APD) operating in the near-infrared (NIR) region. Heterostructure NWs consisted of GaAs and tunable band gap $\text{GaAs}_{1-x}\text{Sb}_x$ serving as the multiplication and absorption layers, respectively. A doping compensation of absorber material to boost material absorption, segment-wise annealing to suppress trap-assisted tunneling, and an intrinsic i-type and n-type combination of the hybrid axial core to suppress axial electric field are successfully adopted in this work to realize a room-temperature (RT) avalanche photodetection extending up to 1.3 μ m. In an APD device operating at RT with a unity-gain responsivity of 0.2–0.25 A/W at ~5 V, the peak gain of 160 @ 1064 nm and 18 V reverse bias, gain >50 @ 1.3 μ m, are demonstrated. Thus, this work provides a



foundation and prospects for exploiting greater freedom in NW photodiode design using hybrid axial and CS heterostructures.

KEYWORDS: core—shell nanowires, avalanche photodiodes, SAM-APD, GaAsSb, hybrid axial/CS NWs, near-infrared, photodetector, non-selective growth, ensemble nanowires, self-catalyzed, VLS/VS growth

■ INTRODUCTION

The infrared detection and imaging technology has grown enormously in the past few decades. Applications include optical interconnects, light detection and ranging, 2,3 autonomous vehicle trackers and atmospheric sensing,2 communication systems, quantum computing, medicine, and astronomy. Semiconductor-based avalanche photodiode (APDs) and p-in heterostructures are the commercially dominant technologies representing the most advancement in this field. III-V semiconductor APDs, dating nearly half a century in history, have recently been shown to have improved gain and sensitivity^{7,8} by shrinking the impact ionization region in the sub-micron heterostructure. Flexibility in design architecture, material choice, and fabrication process are the key driving factors in semiconducting materials compared to alternative superconducting materials in the short-wavelength infrared (SWIR) range. Quantum heterostructure inclusion and nanophotonic resonances¹ provide additional design freedom in this sector.

InGaAs/InP-based single-photon avalanche diodes are one of the most promising candidates in SWIR region photodetection with very low dark currents and high detection efficiency. ^{10,11} Dark count rates (DCRs) as low as 3 kHz, jitter time as low as 30 ps up to $1.6 \,\mu \mathrm{m}$ wavelength, with 45% detection efficiency, have been demonstrated for single-photon detection. ^{4,12} A low dark current of 10-300 nm with a 3dB bandwidth of 80 GHz has

been shown with a thin multiplication layer 13 in this material system. Germanium (Ge)-based APDs are another promising candidate for photodetection in the SWIR region. Multiplication gain as high as 680 at 8 V reverse bias 14 has been reported, enabling 43 Gb/s speed at 1550 nm with a bit-error rate of 10^{-12} . 15

A significant performance improvement over the current planar technologies can be accomplished using lower 1D dimensional nanowire (NW) structures exploiting their unique optoelectronic properties. The small footprint and 1D geometry of the NWs provide further versatility in implementing a wide variety of different architectures and band gap engineering that are not conceivable in thin-film photodetectors. III–V APDs in the ensemble NW configurations exhibit advantages of strain relaxation, ¹⁶ waveguide effects, ^{17,18} and compatibility with the mainstream silicon technology. ¹⁹ Lower breakdown voltage, reduction in the DCR, and jitter time² are the other potential outcomes of reducing to lower dimension geometry structures allowing for higher photon counting rates with room-temper-

Received: August 17, 2022 Accepted: March 6, 2023 Published: March 20, 2023





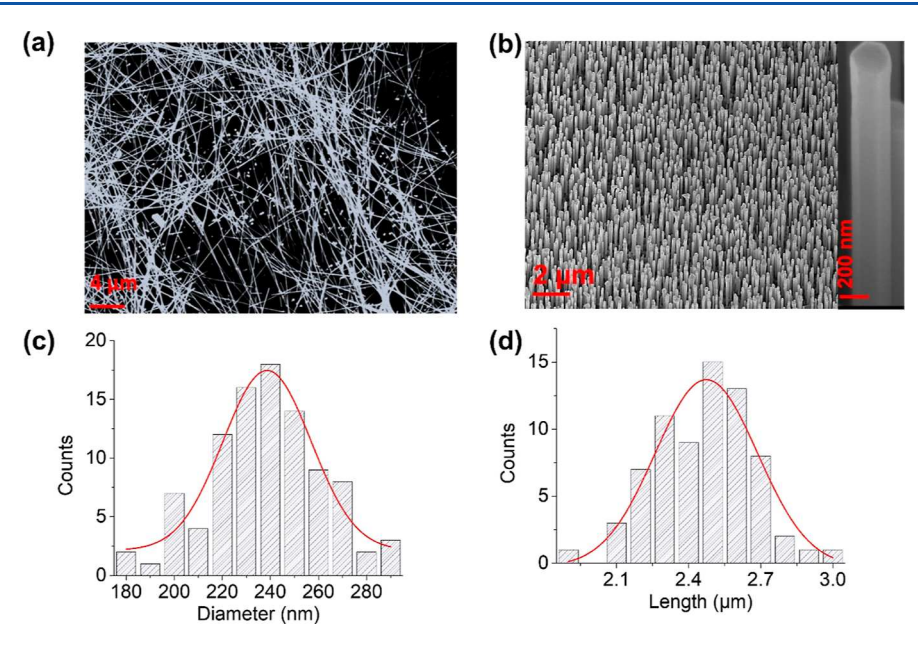


Figure 1. (a) SEM image of top silver (Ag) contacts onto NWs, (b) SEM image of ensemble NWs grown on the Si < 111 > substrate (10% Sb incorporation) with a SNW at the inset, (c) NW diameter distribution, and (d) NW length distribution. Approximately 90 measured NW lengths and 70 measured diameters across the samples are plotted to get a normal distribution.

ature (RT) detection. While the capabilities of nanoscale devices are constantly being pushed, research in III—V semiconductor NWs can propel these advances to new heights using combinations of different material systems and architectures.

NW APDs have been demonstrated in several configurations, namely, single silicon (Si) axial p-i-n NW homojunction, $^{20-22}$ single axial InP with InAsP quantum dots (QDs),²³ crossed p-Si/n-CdS NWs, core-shell (CS) GaAs junction,^{1,24} separate absorption and multiplication (SAM)-based selectively grown axial InGaAs nanopillars (NPs), 25 InGaAs/GaAs NW heterojunction,² InP/InAsP NW heterojunction, ¹⁶ and axial tapered InP arrayed axial p-n junction NWs.²⁶ Farrell et al.² demonstrated work on vertical InGaAs-GaAs NW arrays using the SAM-APD configuration in the near-infrared (NIR) region, revealing the high capability of NW-APD in achieving a low DCR and timing jitter with significantly high photon count rates. A substantial gain value exceeding 104 is reported by Bulgarini et al.²³ in InP semiconductor NW embedded with InAsP QDs, enabling the detection of a single photon in the NIR region. A work on GaAs CS nanoneedle APDs by Chuang et al.²⁴ showcases high avalanche multiplication at RT at a significantly lower breakdown voltage. Parakh et al.²⁷ recently demonstrated an axially configured ensemble of NW APDs, with a low breakdown voltage and significant gain exceeding 200 at RT on an arsenide-antimonide system. It is evident that most of the prior work is dedicated to arsenide material systems, with no reports on antimonide material systems in the CS NW configuration despite its promising application wavelength range in the NIR region.

This paper explores a self-catalyzed, epitaxially grown GaAs/GaAsSb CS-based NW separate absorption, charge control, and multiplication region (SACM) APD for near-infrared (NIR) photodetection. GaAs and GaAsSb material systems in an NW configuration having a single group III element have the advantage of a broader growth window due to the high vapor pressure group V species impinging on the droplet predominantly responsible for the growth, in comparison to the multiple group III material systems with widely different diffusion

lengths. ^{28,29} Furthermore, self-catalyzed GaAsSb NWs have the advantage of phase purity exhibiting only zinc-blende (ZB) crystal structure essentially free of planar defects 30,31 as opposed to polytypism in competitive InGaAs NW counterpart. 32,33 Additionally, a CS architecture enables better passivation and shielding of the active junction from surface disorder and provides a better pathway for strain relaxation, particularly in highly lattice-mismatched heteroepitaxial layers than their axial counterparts.³⁴ Also, CS-configured NWs offer increased device sensitivity due to the decoupling of vertical light absorption and radial carrier generation.³⁷ However, Sb-deficit regions at the tips and interfaces and inhomogeneous composition distribution with a spontaneous CS structure³⁵ are some of the issues of this material system. Despite these problems, large carrier mobilities²⁸ and large spin-orbit coupling³⁶ with superior absorption properties 28,37 in the telecommunication wavelength region, along with exceptional crystal phase purity, add tremendous value to photodetection applications.

In this work, we present a systematic study of GaAs/GaAsSbbased CS NW heterostructure design in achieving RT photodetection up to 1.3 μ m using a tunable band gap GaAsSb absorber material, a wider-band gap GaAs multiplication, and charge control regions. A narrow band gap region for light absorption and a higher band gap multiplication region are designed to enable low noise photodetection. The absorption band of GaAsSb covers the entire telecommunication bands up to the C band (1530–1565 nm), which can be tuned simply by varying the Sb composition. Thus, our CS NW device uses a tunable band gap GaAsSb as the absorber material. The APD heterolayer structure exhibited pure ZB phase free of planar defects over most of the NW length. The composition of $GaAs_{1-x}Sb_x$ corresponds to the band gap range of 1.25 to 0.95 eV, as determined from photoluminescence measurements. Temperature-dependent current-voltage (I-V), capacitancevoltage (C-V), low-frequency noise (LFN) measurements, and intensity dependence of photocurrent measurements are utilized to get more insights into the material and interface traps and their effects on the nature of the breakdown

mechanisms. These were then used to suppress the band-to-band tunneling responsible for Zener breakdown in the nanoscale-wide heterostructures via judicious 3D heterostructure design to impact the ionization process with improved photodiode performance.

EXPERIMENTAL DETAILS

Samples were grown on an epi-ready n-type Si (111) substrate via the vapor-liquid-solid (VLS) mechanism by molecular beam epitaxy (MBE) using As₄ and Sb₂ species at a varying growth temperature from 550 to 615 °C. The Ga cell temperature and arsenic (As) cracker cell temperature set for As₄ species were preset to a beam equivalent pressure (BEP) group V/III ratio of 10 to yield a nominal GaAs thinfilm growth rate of 0.25 monolayer/second (ML/s). Ga pre-deposition of 10 s was used for self-catalyzed growth. The GaAs core was grown at a temperature of 600 °C at a BEP ratio of 10, followed by intrinsic and Bedoped GaAs segment growth at 550 °C at a BEP ratio of 12. The substrate temperature was increased to 590 °C for the GaAsSb absorption layer and the growth of the highly p-doped GaAsSb contact layer. The Sb composition of the GaAsSb layer varied from \sim 5 to \sim 30 at. %. The composition estimation is based on the extensive prior work of our group on detailed measurements of composition versus lowtemperature photoluminescence variation in the CS configuration.³⁸ Finally, a low-doped passivation layer of AlGaAs was grown at 465 °C for 8 min, followed by an intrinsic GaAs segment growth for 2 min. A Su-8 polymer was spin-coated and etched to the desired height to expose NW tips before the chemical treatment to remove the passivation layer. Silver (Ag) NW contacts (Figure 1a) to the exposed NW tips and silver paste on the bare Si surface served as top and bottom contacts, respectively, such that an ensemble of NWs is contacted in parallel.

The optical characteristics of NWs were investigated using microphotoluminescence (µ-PL) at RT and 4 K on a low-vibration closedcycle optical cryostat from the Montana Cryo-station using a 633 nm He-Ne laser excitation source. The surface morphology of NWs was characterized using Carl Zeiss Auriga-BU FIB field emission scanning electron microscopy (SEM). I-V characteristics of ensemble NWs were obtained using two probe Keithley-4200 semiconductor parameter analyzer systems integrated with a radiation shield equipped with a Lake Shore TTPX probe station. A microHR (LSH-T250) Horiba spectrometer equipped with a tungsten-halogen lamp excitation source was used for studying the spectral photo-response. The optical illumination area of 0.2 cm² is assumed to be representative of our device contact area. Finally, a LFN setup consisting of two independent low-noise current preamplifiers and a dynamic signal analyzer were used to measure the LFN. The measurements were carried out from 1 to 3200 Hz, and the data were averaged over 100 sets of readings. The capacitance-voltage measurement was performed using a Keithley 4215-CVU low-noise capacitance unit capable of measuring frequencies from 10 kHz to 10 MHz. It is to be noted that an AC signal of 30 mV and 1 MHz is applied for a typical capacitance measurement of our devices. COMSOL Multiphysics Finite Element Method (FEM) simulations have been performed for a range of doping and NW segment thicknesses for the proposed NW structure to get an estimate of the electric field (E-field) in the heterostructure. Highresolution scanning transmission electron microscopy (HRSTEM) images, transmission electron microscopy (TEM) images, selected-area diffraction patterns (SAED), and energy-dispersive X-ray spectroscopy (EDS) elemental maps were acquired on a probe-corrected Thermo Fisher Titan G2 operated at 200 kV. EDS maps were acquired with a probe current of ~250 pA. EDS maps were processed to subtract the background using standardless techniques in Velox. HRSTEM images were acquired using both bright field and dark field detectors. The probe semiconvergence angle was measured at ~19 mrad.

APD Device Design. A separate absorption of GaAsSb with varying Sb composition, a charge sheet layer of p-GaAs, and a higher band gap GaAs multiplication region was used in a CS configuration. The composition of Sb in the GaAsSb region ranged from 7 to 30 at. % to tune the absorption wavelengths in the APD structure from 0.95 to 1.3

 μ m, corresponding to a band gap PL emission range of ~1.25 to ~0.95 eV (Supporting S1c). An optimum doping concentration and segment thickness were extracted from E-field simulations (using COMSOL Multiphysics) of the structures of varying segment thicknesses and doping profiles (Supporting S2) that would provide *E*-field strength >1 \times 10⁵ V/cm in the multiplication region to initiate the avalanche mechanism. ^{1,40} The doping density of each segment was calculated experimentally using a combination of X-ray photoelectron spectroscopy/ultraviolet photoelectron spectroscopy (XPS/UPS) and conductive atomic force microscopy (C-AFM)/scanning Kelvin probe microscopy based on our earlier work by Ramaswamy et al.41,42 and Devkota et al.⁴³ The Be- and Te-doping density of different segments was estimated using a combination of XPS/UPS, 42,44 from quantifying the corresponding shift in the Fermi level toward the valance and conduction bands, respectively. These values were further confirmed from electron/hole densities computed from I-V characteristics of C-AFM measurements of the single nanowire (SNW). The overall accuracy of the doping density of SNW is estimated to be $\pm 5\%.^{34,35}$ The individual axial segment growth rates were calculated from SEM images performed on segment-wise CS APD structure growth, as shown in Supporting S3.

A radial thickness of GaAs n-core of $\sim 35-40$ nm has been selected based on the optimized growth conditions of n-core on the n-Si < 111 > substrate. Similarly, the choice of doping density of 2.0×10^{18} /cm³ for the n-GaAs core is representative of the optimized Te-doping conditions that yielded the best NW optical properties and verticality. The thicknesses and doping of i-GaAs, p-GaAs, and GaAsSb absorber regions have been tuned to minimize the breakdown voltage in the NW device within the possible growth limits. The simulated *E*-field profile along the radial direction and *E*-field profile of the device at 0 and 14 V reverse bias, for ~ 20 nm radial thickness of the multiplication region, can be found in Supporting S4. The simulated value of the *E*-field is about 5×10^5 V/cm, which is sufficient to initiate the avalanche mechanism in the GaAs material at a reverse bias ≥ 14 V. Further decrease in the thickness resulted in a significant deviation from APD I-V characteristics due to an increase in tunneling current.

The details of the designed GaAsSb/GaAs CS SACM APD structures are summarized in Table 1, and a typical SEM image of as-

Table 1. Device Structure Details

material	doping (cm^{-3})	radial thickness (nm)
GaAs	$5.0 \times 10^{18} (\text{n+ -type})$	35-40 nm (core)
GaAs	undoped	20-40 nm (intentionally varied)
GaAs	$7.0 \times 10^{17} (\text{p-type})$	10-15 nm
GaAsSb	$7.0 \times 10^{16} (\text{p-type})$	20-35 nm (intentionally varied)
GaAsSb	$7.0 \times 10^{18} (p+ -type)$	5-10 nm
AlGaAs	undoped	10-15 nm
GaAs	undoped	5-10 nm

grown APD NWs is shown in Figure 1b. The average length and diameter of NWs were 2.5 μ m and 240 nm, respectively. The distribution of NW diameter and length in the samples is shown in Figure 1c,d, respectively.

Figure 2a shows a schematic of the proposed CS structure. A schematic of the band profile along the radial direction (as shown in Figure 2b) of designed SACM-APD NWs at zero bias and reverse bias conditions are shown in Figure 2c,d, respectively.

■ RESULTS AND DISCUSSION

First, the avalanche characteristics of the structure shown in Figure 2a are presented and analyzed. This is followed by the study on segment-wise annealing on each grown segment of the APDs to suppress the trap-assisted transport mechanism and improve device stability. Finally, tuning of the breakdown voltage via judicious modification of the 1D heterostructure and spectral wavelength tuning with increased Sb incorporation in

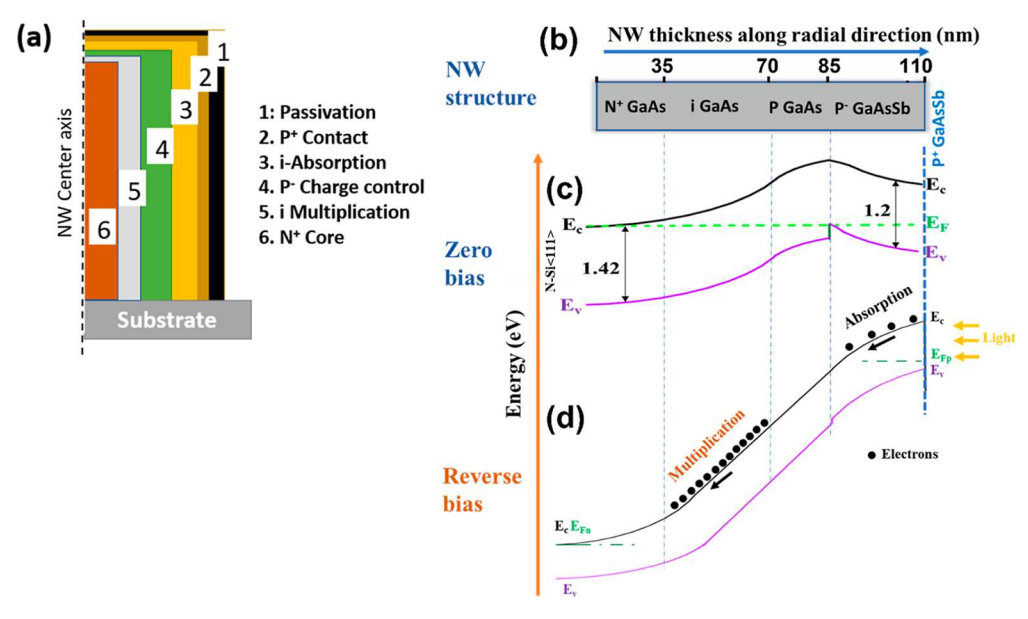


Figure 2. (a) NW structure schematic, (b) NW composition along the radial direction, (c,d) band diagram at zero bias and reverse bias \geq 20 V conditions, respectively, drawn for an Sb composition of \sim 10 atomic %.

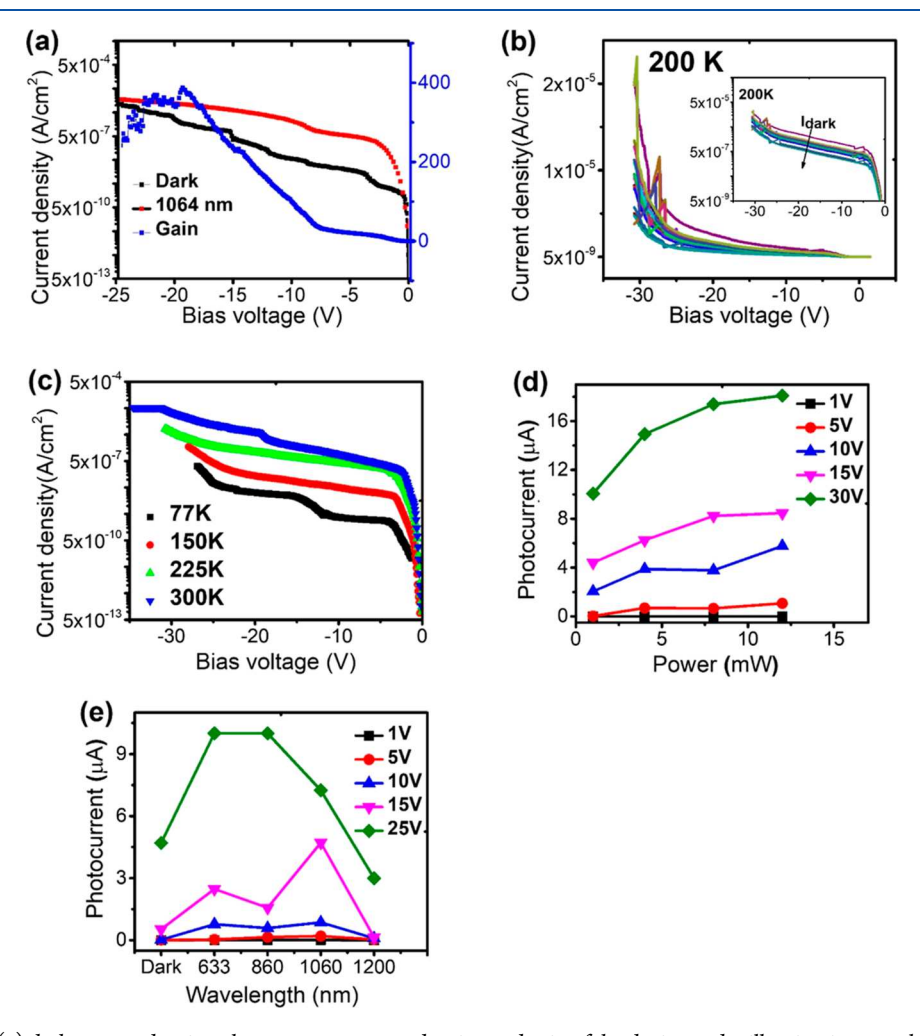


Figure 3. R10 sample: (a) dark current density, photocurrent current density, and gain of the device under illumination wavelength of 1060 nm at 200 K, (b) multiple dark I-V sweeps at 200 K showing the range of hysteresis, (c) temperature dependence of dark current density at multiple temperatures from 77 to 300 K, (d) power dependence of the device for a range of illumination power and bias voltage at 633 nm illumination wavelength at 200 K, and (e) spectral response of the device at 200 K at a range of voltage from 1 to 25 V.

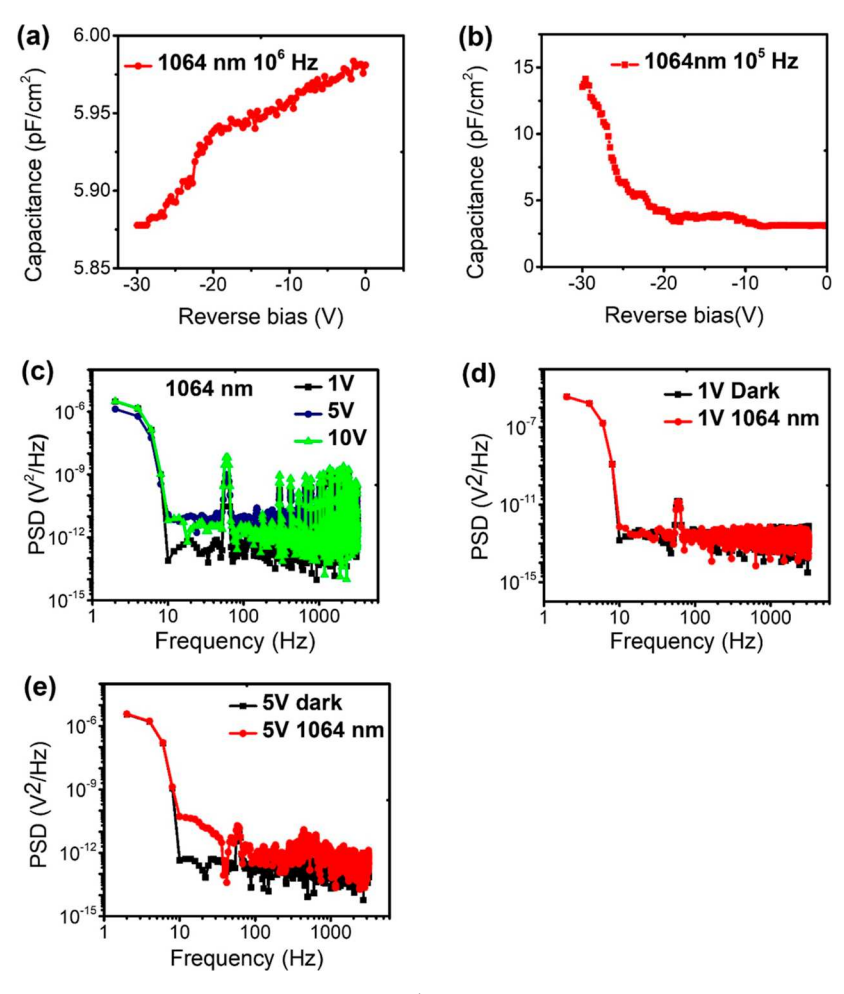


Figure 4. Capacitance—voltage measurements of the R10 device at (a) 10⁶ Hz and 30 mV AC power at 200 K and (b) 10⁵ Hz and 30 mV AC power at 200 K. (c) Comparison of device noise under 1064 nm illumination conditions and (d,e) dark and illumination noise at 1 and 5 V reverse bias, respectively.

the absorption region is discussed. A study on four representative APD NWs is discussed below.

■ AVALANCHE CHARACTERISTIC STUDY: R10

The characteristic features of the first reference sample SACM-APD device referred to as R10, reported in the first part of this work, correspond to a core n-GaAs core diameter of 35 ± 5 nm, a radial multiplication thickness of 25-30 nm, a p-GaAs charge control layer of 12 ± 3 nm, and an absorption layer thickness of 25 ± 3 nm with an Sb incorporation of ~ 10 at. %.

The I-V characteristics of the R10 sample are shown in Figure 3a under dark and illumination of 1064 nm monochromatic light at 200 K. A low dark current of ~10 nA is observed at the punch-through voltage of ~5 V, which gradually increased to \sim 10 μ A before the onset of breakdown at approximately 30 V at 200 K. The current compliance of the system was set to approximately near breakdown voltage (V_{BR}) to prevent high current flow and thus damage to the device. It is to be noted that dark current at a unity-gain voltage of ~1.8 V was taken in gain computation, and the dark current value, including persistent photocurrent increase in the illuminated *I*– V characteristics, was considered in the gain calculation (refer to Supporting S5a for observed persistent photocurrent with 633 nm laser illumination). For a temperature of 200 K, an approximate gain of over 300 is estimated under 1064 nm light illumination with an intensity of $\sim 8 \text{ mW/cm}^2$, as shown in

Figure 3a. The gain curve exhibits a small gain up to \sim 8 V reverse bias, after which an exponential increase in gain was observed. This indicates that the generation of photocarriers is not dominated by impact-ionization, but by photo-absorption up to 8 V reverse bias, beyond which the *E*-field strength is sufficient to initiate the exponential impact ionization process. A unity-gain responsivity of 0.2-0.25 A/W is achieved at ~1.8 V, which is higher than reported values for pure GaAs NWs44 and comparable to the GaAs NW APDs. 1,45 The computation of device responsivity in this work is discussed elsewhere. 46 It was noted that the device showed a marginal increase in dark current after shining light, and we attribute this observation to the trap filling on illumination and slow release of carriers by the traps thereafter under dark DC sweep (Supporting S5a). Figure 3b shows the result of repeated DC voltage sweeps on $V_{\rm BR}$ at 200 K. A considerable fluctuation in the breakdown voltage is observed during the initial sweeps, with the fluctuation range decreasing and a decrease in dark current on repeated DC I-V sweeps (inset as shown in Figure 3b).

Breakdown characteristics from 150 to 250 K under dark conditions (Figure 3c) reveal a positive temperature coefficient, a signature of an avalanche breakdown mechanism. The photocurrent cut-off wavelength of 1060 nm is consistent with the RT PL spectral peak observed on this sample (Supporting S1a). At 200 K, a dark current of \sim 10 μ A is observed at the breakdown voltage. A temperature coefficient of \sim 10 mV/K is

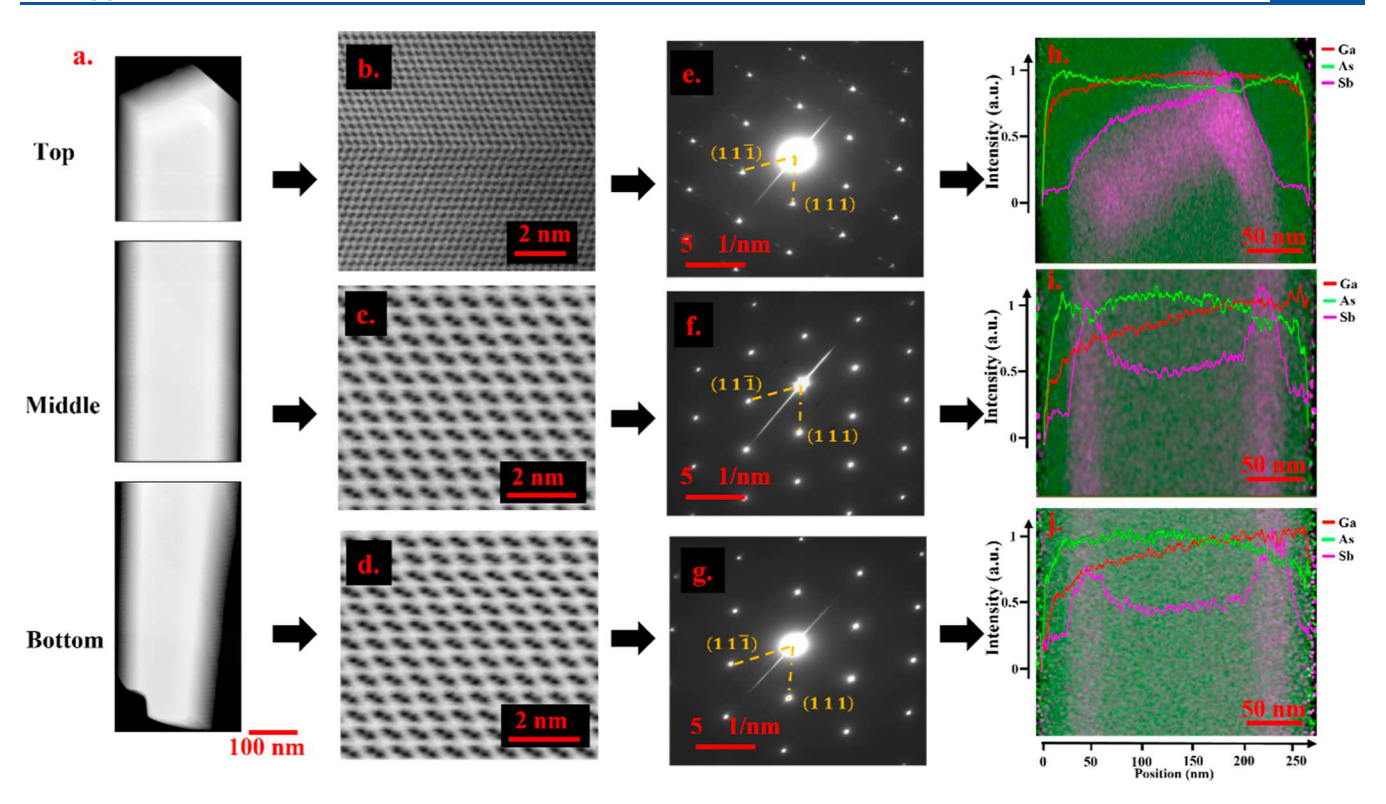


Figure 5. Top, middle, and bottom of S10 APD NW segments: (a) TEM images, (b-d) HRTEM images, (e-g) SAED patterns, and (h-j) HAADF STEM with false-color EDS mapping superimposed and EDS elemental line scans.

observed up to 225 K, close to the reported temperature coefficient in GaAs.^{2,47} A negative dependence on breakdown observed at a temperature exceeding 225 K indicates the dominance of the tunneling mechanism over the impactionization generation mechanism. A shift of 5-10 V in $V_{\rm BR}$ toward higher voltage is noted after initial sweeps with minimal change in repetition thereafter (Supporting S5b). The sizeable initial shift in $V_{\rm BR}$ with I-V sweeps is attributed either to annealing of the NW and NW/contact interface and/or burning of very low diameter NWs present under an NW contact, resulting in near-consistent I-V characteristics stabilizing at lower dark current (refer Supporting S5a for the observed hysteresis at the beginning compared to the stable operation of the device). The effect of annealing is consistent with similar changes reported in the avalanche characteristics of the InP/ InAsP APD device by Jain et al. 16 At 250 and 77 K, the variation in breakdown characteristics was found to be in the range of 30 \pm 3 and 25 \pm 4 V, respectively. We attribute this $V_{\rm BR}$ variation to contributions from (i) the non-uniformity in the thickness of the grown NW samples (as shown in Figure 1b,c) and (ii) doping variation among the segments in ensemble NWs. One or both possibilities can profoundly affect the threshold E-field required for the onset of punch-through and the $V_{\rm BR}$ of the device. Furthermore, the trap filling after the initial sweep factor also contributes to the observed variation in V_{BR} . The overshooting observed in a few scans at ~27 V, as shown in Figure 3b, is speculated to be the effect of burning of comparatively lower diameter NWs under repeated I-V scan, which is also manifested in the observed shifting of V_{BR} toward higher voltage with the increasing number of scans (inset 3b). The power dependence of photocurrent characteristics is given in Figure 3d, which shows a linear increase in photocurrent with illumination power. For higher bias voltage, an indication of saturation of absorption in NWs was observed at an illumination power ≥7

mW, which may be a result of increased carrier recombination and lateral spreading of the photoexcited carriers due to the presence of traps. Lower variation in breakdown voltage was observed at higher temperatures, revealing the dominance of the generation-current component over the band-to-band tunneling as expected.² The wavelength dependence of APD devices (Figure 3e) at different reverse bias voltages exhibited good photo absorption up to 1064 nm with the cut-off after 1100 nm. It is to be pointed out that device failure occurred for the illumination power >15 mW and for reverse bias voltage exceeding 30 V.

The C-V characteristics at 300 K did not reveal any clear capacitance variation trend with voltage and are hence not shown here. At 200 K and under 1064 nm illumination (Figure 4a), a gradual decrease in capacitance with reverse bias indicates the progressive depletion of the charge layers. At 25 V reverse bias, rapid change of device capacitance is a signature of rapid channel depletion and increased carrier multiplication. Invariant and stable capacitance for frequency above 400 kHz is a true representative of the device capacitance value as the impedance across the capacitance will be lower at these frequencies. However, at lower frequencies (Figure 4b shows the C-V at 100 kHz), the ac impedances of resistors and capacitors become comparable, and the C values are not a true representative of the device capacitance (Figure 4b). LFN characteristics were also examined under dark and illumination settings for a reverse bias up to 10 V (see Figure 4c-e). A clear increase in the average noise level was observed with increasing bias under illumination, especially above the punch-through voltage compared to below punch-through (<5 V). A change in the noise level is observed only after likely punch-through (see Figure 4d,e) due to increased randomness of the carriers via enhanced generationrecombination (G-R) noise. A signature of 60 Hz noise from

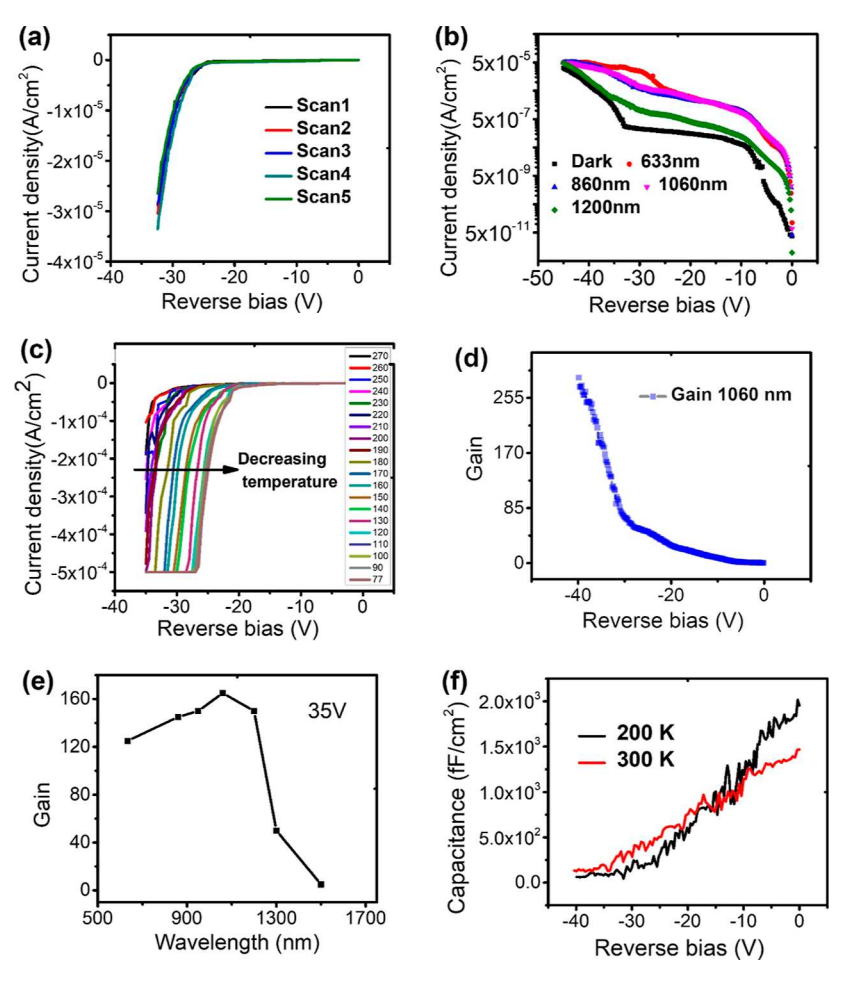


Figure 6. S10 sample: (a) five repeated dark I-V measurements of the device at 300 K temperature and (b) I-V measurements for different illumination wavelengths up to 1200 nm. (c)Temperature dependence of the NW device with multiplication region thicknesses of ~35 nm, (d) gain of the device with reverse bias at 1060 nm wavelength, (e) measured gain of the device with wavelength for a reverse bias voltage of 35 V, and (f) capacitance—voltage measurements of the device at 200 and 300 K temperatures.

the source panel is observed in the LFN characteristics in Figure 4c-e

■ EFFECT OF SEGMENT-WISE HETEROSTRUCTURE ANNEALING: S10

The effects of annealing on the device characteristics were studied under ultra-high vacuum @ 1.5×10^{-10} Torr ambient for each grown NW segment on the device characteristics. Segmentwise in situ annealing of the heterostructure NWs for 120 s was adopted along with post-growth in situ annealing at 465 °C for 5 min. The i-GaAsSb layer segment was compensated with n-type Te-doping for 5 s over a 1 min interval to achieve lower intrinsic doping in the region. The details of compensation for the intrinsic p-nature of GaAsSb for the enhancement of absorption and material properties are discussed elsewhere.⁴⁸ The compensation of the Sb absorber region and hence the increase in absorption efficiency were marked by a substantial increase in the responsivity and external quantum efficiency. 48 This sample with ~ 10 at. % Sb incorporation in the absorption region combined with segment-wise annealing shall be referred to as S10 hereafter.

A TEM image of representative APD NW is shown in Figure 5a. Figure 5b-g represents the HRTEM images and corresponding SAED patterns for the NW top, middle, and bottom segments, respectively. The bottom and mid segments

exhibit < 111 > oriented pure ZB crystal phases with no planar defects, for example, stacking faults, indicative of the superior structural and interfacial quality of the multilayer APD NW heterostructure and absence of dopant segregation. This may be considered evidence of the success of our growth pauses and annealing process approach after each segment in samples S10, S10T, and H30. However, the NW tip is characterized by planar defects, primarily twins, as evidenced by the HRTEM image. The high defect density at the tip is manifested in the broadening of the center electron beam spot in the corresponding SAED pattern. The deteriorating interfacial quality is most likely associated with a remnant Ga droplet, leading to continual axial growth and shell growth. High-angle annular dark-field scanning TEM (HAADF STEM) imaging overlaid with false-color EDS mapping (Figure 5h-j) and analogous compositional line scans for both the bottom and mid segments shows clearly the CS geometry delineating the GaAsSb absorption layer, as confirmed by the color contrast and Sb-rich region at the NW outer shells along the radial direction; these can be compared to the schematic of the growth structure in Figure 2a. As these are atomically "thick" NWs, delocalization of the EDS signal due to probe broadening is expected to result in the interface broadening. Furthermore, the Sb atomic percent is significantly lower than the expected Sb 10 at. % due to the X-ray signal emanating from the large interaction volume spanning adjacent

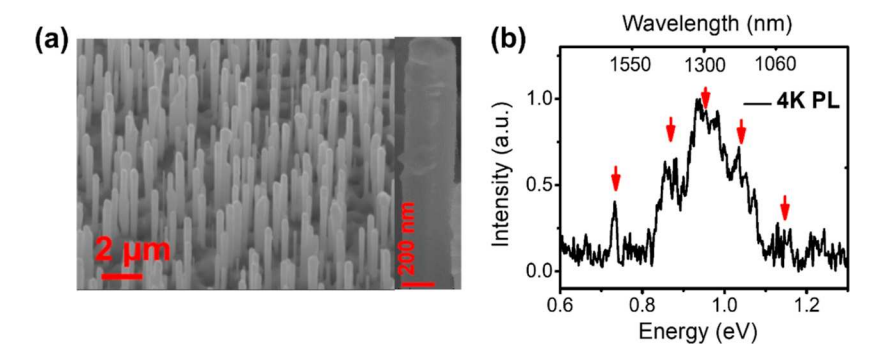


Figure 7. (a) SEM image of SACM-APD for Sb incorporation of \sim 30% into the absorption region with the SNW image in the inset and (b) corresponding 4 K photoluminescence showing multiple GaAsSb-related peaks centered around 0.95 eV.

GaAs layers, which provides an average composition. Similarly, the lack of the Al peak at the outermost passivation layer is due to a very thin passivation outer layer, possibly couple of monolayers, coupled with the software attempting to do the compositional analysis on the adjacent vacuum area. The TEM images of more representative NWs from random multiple NWs are included in Supporting S6 and demonstrate the typical variation observed in NW structures.

The I-V characteristics, gain spectral response, and C-V measurements of the S10 devices thus obtained are shown in Figure 6.

Increased repeatability of I-V characteristics with a reduction in hysteresis (Figure 6a) under dark conditions and minimal change in the breakdown characteristics are the improvements of this device over the R10 sample (Figure 3b). These indicate a trap state reduction in the heterostructure interfaces with segment-wise growth annealing. The device showed spectral sensitivity up to 1100 nm (as shown in Figure 6b,e). A positive temperature coefficient of $\sim 30 \text{ mV/K}$ of V_{BR} in the reverse bias *I–V* characteristics observed over a broader temperature range of 77-300 K, as shown in Figure 6c, attests to avalanche characteristics. We hypothesize that the increase in the temperature coefficient of breakdown voltage from sample R10 to S10 is caused by dopant redistribution/diffusion in the multiplication segment with annealing. Since the length of the multiplication region is very thin (\sim 25–30 nm radially), a slight change in the dopant distribution can induce a substantial fluctuation in the device characteristics. A device gain exceeding 150 at 1060 nm wavelength at RT is achieved at reverse bias exceeding 35 V (Figure 6d,e). To confirm avalanche characteristics, C-V measurements were taken at two temperatures of 200 and 300 K (see Figure 6f), which showed an increase in the device breakdown, suggesting slower depletion of the NW channel with the temperature rise.

■ V_{BR} AND ABSORPTION WAVELENGTH TUNING: S10T AND H30

To further lower the breakdown voltage of the NW APDs, a thinner multiplication layer of GaAs (20–25 nm) was examined to augment the critical *E*-field intensity for impact ionization (Supporting S7). However, a reduction of the multiplication thickness below 25–30 nm resulted in a large device dark current beyond punch-through and the disappearance of avalanche breakdown characteristics at RT (Supporting S8) due to enhanced tunneling probability. This sample shall be referred to as S10T hereafter. It is to be noted that significant contribution from the axial *E*-field is very likely in the thin multiplier sample (S10T) and earlier designs [original sample

(R10) and segment-wise annealed sample (S10)] as the thicknesses of radial and axial growths are expected to be comparable during vapor-solid (V-S) growth of the shells. It is very likely; as this is an ensembled NW device, the absence of reflected flux from the substrate, as shown by Sharma et al. 49 in the modeling of GaAsSb-patterned NW arrays, the axial growth can be lesser than radial growth and hence can provide a dominant path for carrier multiplication. This becomes more pronounced for smaller multiplication thicknesses as the *E*-field through the axial structure can become very high compared to the radial E-field, triggering Zener breakdown. Therefore, an intentional i-GaAs layer of ~400 nm was axially grown on top of the n-core GaAs region to suppress the axial E-field strength through the top segment of NW heterostructure and for better radial *E*-field confinement. A schematic and *E*-field distribution for this new design can be found in Supporting S4. Compared to the original (R10) and segment-wise annealed (S10) samples, an apparent decrease in the axial E-field toward the absorber region is achieved with this design (refer to Supporting S2 and S4 for comparison). A new architecture showed a reduction in axial E-field strength, thus lowering the contribution of axial carrier multiplication and/or tunneling in the presence of a high E-field. This design lowered the avalanche breakdown voltage to $18 \pm 3 \text{ V}$ at RT for the multiplication layer GaAs thickness of \sim 20–25 nm. Successful validation of the proposed change in the NW APD structure is shown via the change in I-Vcharacteristics and illumination-dependent I-V characteristics, as shown in Supporting S9 (compared to S8) and referred to as H10 sample.

To further extend the spectral sensitivity beyond 1300 nm, the Sb/As flux ratio was increased in the absorption layer. This sample represents $\sim\!30$ at. % Sb incorporation into the absorption region with a thinner multiplication region of 20–25 nm; segment-wise annealing shall be referred to as H30 hereafter.

SEM images and corresponding 4 K PL band emissions observed for this sample are shown in Figure 7a,b, respectively. An increase in 2D growths and an NW diameter increase of 15 ± 3 nm for the same growth duration are characteristic of increased Sb incorporation into the absorption region. 4 K PL exhibits a redshift consistent with band gap reduction for higher Sb concentration with a broad peak consisting of multiple GaAsSb-related peaks spanning from 0.85 to 1.05 eV (Figure 7b). The low intensity and the presence of multiple peaks are attributed to the Sb-related defects originating from the impingement of high Sb flux and the stress arising from the lattice mismatch between the GaAs and GaAsSb, which has been discussed in detail in our earlier work. 38,50 The compositional variation in the grown

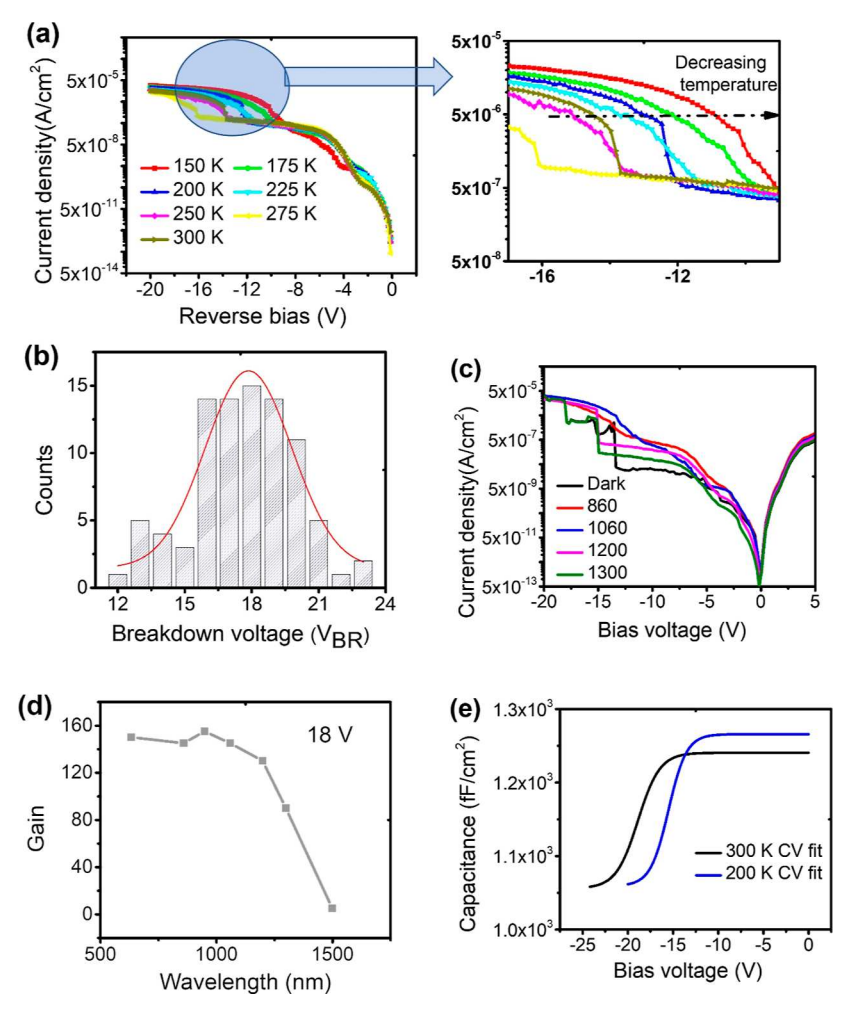


Figure 8. H30: (a) temperature dependence of the NW device dark I-V: inset shows the enlarged breakdown region at different temperatures and (b) breakdown voltage distribution of dark I-V measurements of the device at 300 K temperature for \sim 90 measurement spots. (c) Voltage-dependent dark and illumination I-V measurements of the devices up to 1300 nm wavelength, (d) gain measurements at 18 V reverse bias corresponding to voltage-dependent photocurrent measurements, and (e) fitted capacitance—voltage measurements of the device at 200 and 300 K (refer to Supporting S10 for the original fit of the data).

structures in the presence of high Sb flux is found to cause such features elsewhere. $^{\rm S1}$

The temperature dependence of the I-V characteristics under dark conditions, ranging from 150 to 300 K (Figure 8a), shows a positive temperature coefficient of ~35 mV/K. An increase in the temperature coefficient was observed compared to the previous segment-wise annealed sample (S10). This effect is attributed to the possible increase in the dead space effect³² and radial *E*-field, resulting from multiplication thickness reduction and axial E-field suppression. All of these factors are likely to change the ionization probability, and the contribution of each can be a subject of further study. An increase in the dark current magnitude by 1 order was observed, which is attributed to a much lower band gap absorption region in this thinnermultiplier region and high Sb composition (H30) sample, resulting in increased band-to-band tunneling through the segment and thus the dark current. Figure 8b shows the result of numerous dark scans at different spots of the NW sample, with the breakdown voltage fluctuating by ~3 from 18 V. Few premature and higher voltage breakdowns are observed at a few spots due to the unavoidable inconsistency of NW diameters and parasitic growth in non-patterned ensemble NW growth. The spectral I-V measurements of the device (Figure 8c,d)

showed a gain response up to an illumination wavelength of 1200 nm and tapering off rapidly beyond 1300 nm. C-V characteristics (Figure 8e) at 1200 nm under illumination carried out at two different temperatures, 300 and 200 K, exhibited a breakdown at ~20 and ~17 V reverse bias, beyond which the device capacitance remained invariant with further bias increase. The C-V characteristics of the device support the positive temperature coefficient observed in the corresponding I-V plots.

Voltage-dependent LFN measurements of the device under the dark are shown in Figure 9. At 300 K, a significant increase in noise was seen with increasing reverse bias, flanked by G–R noise exhibiting Lorentzian characteristics at lower frequencies and a 1/f dependence at higher frequencies, attributed to the presence of traps in the device (Figure 9a). The 1/f noise at 150 K exhibited weak bias dependence at voltages exceeding 5 V, indicating punch-through voltage. An increase in multiplication noise at a lower temperature (150 K) was markedly indicated by a significant increase in G–R noise and a change in 1/f noise characteristics of the device. The difference in the noise characteristics with temperature is a likely effect of the reduction in the thermal carrier density present in the carrier-multiplication path and trap activation. At lower temperatures, the

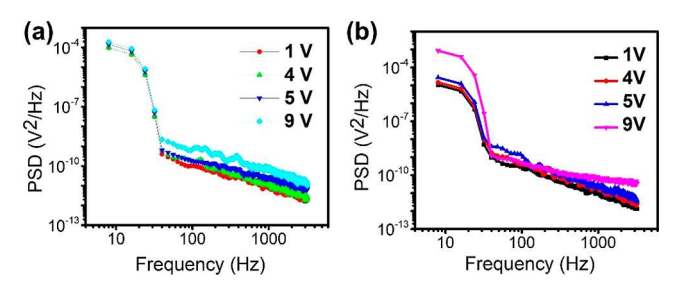


Figure 9. H30 LFN of the APD for different reverse bias voltages at (a) 300 and (b) 150 K.

freeze-out of deeper trap states can also have a role in lowering the *E*-field to deplete the NW and, thus, decrease the punchthrough voltage. This explains the dominance of multiplication noise manifesting as less frequency-dependent noise at bias exceeding \sim 5 V (Figure 9b) in this APD sample. A significant increase in G-R noise at a lower frequency at \geq 6 V reverse bias is speculated to be the contribution of the trap activation from a discretized energy level of a certain depth. The deterministic role of thermal carriers and trap activation with temperature on the NW channel depletion and avalanche multiplication characteristics is another significant aspect that needs further study. Also, it is to be noted that system limitations impaired noise measurements at a bias exceeding 9 V. The devices studied in this work and their characteristics are summarized in Table 2.

A RT APD with a breakdown voltage of ~18 V and broad spectral sensing from 633to 1300 nm wavelength is achieved with ~30% Sb incorporation into our devices. While the observed gain and spectral sensing are significant, the observed $V_{\rm BR}$ is much higher than that reported in the literature in vertical ensemble NW APDs. ^{1,24,27} Further decrease in device dark current and device consistency features is possible via pattered growth of these heterostructures. Since the growth mechanism of the NWs is non-selective, axial variation in the thickness of individual growth segments can be pronounced due to the shadowing effect,⁵³ along with thickness disparity among the NWs. All these can lead to more complex 3D *E*-field fluctuation, deviating from the ideal E-field profile shown in figure Supporting S2 and S4. Such thickness variation has also been reported for patterned NW growths.⁵⁴ A significant change in the confinement energy is reported on NW QWs for a much smaller NW thickness of ~5 nm with the change in NW diameter.⁵⁵ Although we do not expect significant carrier confinement in our layers due to the much larger layer thickness, marginal smearing of the interfaces can be expected. Nonuniformity in absorption layer thickness and composition, especially for higher Sb incorporation, as evidenced by larger PL spectral FWHM observed in our NWs (Figure 7b), are other contributing factors leading to non-uniform light absorption in these NWs and variation in the $V_{\rm BR}$ observed at different contact

sites, limiting the APD device performance. All these detrimental effects can be suppressed in site-selective NW growths. A study of the nature and roles of defects in the complex architecture, intending to reduce tunneling components, is essential to lower the device's dark current for improving the device sensitivity. Additional device engineering architecture implementation is possible with plasmonic field confinement, high band gap blocking layers, and impact ionization engineering. Fitting the noise data with the GaAs device model would provide better insights into the different carrier recombination mechanisms and mitigation of CS interface traps. Furthermore, investigation on optimization of ohmic contacts, and simulation study of the dead-space effect exploiting novel designs in our heterostructure, is crucial to achieving low photon flux detection in the NIR region.

CONCLUSIONS

In summary, we present a study on achieving avalanche breakdown and spectral sensing up to 1.3 μ m by tuning the Sb composition in the GaAs/GaAsSb CS NW SACM-APDs on a Si substrate in the ensemble configuration for the first time. Guided by simulation and a systematic approach to experimental optimization in tuning the breakdown voltage and suppressing the axial carrier tunneling in the CS architecture led to the successful demonstration of an NW SACM APD. Annealing proved to be the key to limiting the interfacial traps in the CS APD architecture. The body of the multilayer NWs exhibited a pure ZB phase with no planar defects, except for a small region around the tip. The experimental optimization of heterostructure annealing and a hybrid NW core design led to a mean RT breakdown voltage as low as ~18 V with a positive temperature coefficient of 35 mV/K. RT gain reached 160 at 1.1 μ m and 50 at 1.3 μ m at 18 V, with a responsivity of 0.2–0.25 A/ W at a punch through of ~5 V. The avalanche breakdown mechanism in the NWs was confirmed using the temperaturedependent I-V and C-V characteristics. The C-V measurements yielded a maximum capacitance of a few hundred femtofarad under reverse-biased conditions, which is an important consideration for high-speed applications. These show the viability of the GaAs/GaAsSb material system utilizing hybrid axial and radial design features as a promising candidate for achieving high-performance nanoscale APDs.

ASSOCIATED CONTENT

Supporting Information

The Supporting Information is available free of charge at https://pubs.acs.org/doi/10.1021/acsanm.2c03644.

PL spectrum of samples under study; *E*-field distribution of R10 CS-APD sample; SEM images of subsequent N-doped, I-doped and P-doped (NIP) growth stages of NWs; *E*-field distribution of the modified structure CS-

Table 2. Summary of Performance Metrics for the APD Devices under Study

sample description	Sb incorporation (at. %)	$V_{ m BR}$	multiplication layer thickness	maximum gain	cut-off wavelength
R10 (reference sample)	10%	~30 V @ 200K	25-30 nm	>100 at -20 V and 1060 nm (200 K)	1.1 μm
S10 (S10 with segment-wise annealed)	10%	~35 V @ RT	25-30 nm	>250 at-35 V and 1060 nm	$1.1~\mu\mathrm{m}$
S10T (S10 with reduced multiplication layer thickness)	10%		20-25 nm		
H30 (S10T with hybrid device architecture and increased Sb incorporation)	30%	~18 V @RT	20-25 nm	>150 at 18 V and 1060 nm> 50 at 18 V and 1300 nm	$1.3~\mu\mathrm{m}$

APD sample, H30; $V_{\rm BR}$ change in unannealed NW APDs with DC IV sweeps; EDS and HRTEM images of S10 representative samples; *E*-field intensity plots for multiplication region thickness and N-segment doping variations; dark DC IV sweeps and wavelength-dependent features of S10-T samples; dark and wavelength-dependent DC IV features of H10 samples; voltage-dependent CV characteristics of H30 samples; and contact performance distribution of CS-APD NW devices (PDF)

AUTHOR INFORMATION

Corresponding Author

S. Iyer — Department of Nanoengineering, Joint School of Nanoscience and Nanoengineering, North Carolina A&T State University, Greensboro, North Carolina 27411, United States; orcid.org/0000-0002-8163-9943; Email: iyer@ncat.edu

Authors

- Rabin Pokharel Department of Nanoengineering, Joint School of Nanoscience and Nanoengineering, North Carolina A&T State University, Greensboro, North Carolina 27411, United States; orcid.org/0000-0002-9935-3863
- Hirandeep Kuchoor Department of Nanoengineering, Joint School of Nanoscience and Nanoengineering, North Carolina A&T State University, Greensboro, North Carolina 27411, United States
- Mehul Parakh Department of Nanoengineering, Joint School of Nanoscience and Nanoengineering, North Carolina A&T State University, Greensboro, North Carolina 27411, United States
- Shisir Devkota Department of Nanoengineering, Joint School of Nanoscience and Nanoengineering, North Carolina A&T State University, Greensboro, North Carolina 27411, United States
- Kendall Dawkins Department of Nanoengineering, Joint School of Nanoscience and Nanoengineering, North Carolina A&T State University, Greensboro, North Carolina 27411, United States
- Priyanka Ramaswamy Department of Electrical and Computer Engineering, North Carolina A&T State University, Greensboro, North Carolina 27411, United States
- Jia Li Department of Nanoengineering, Joint School of Nanoscience and Nanoengineering, North Carolina A&T State University, Greensboro, North Carolina 27411, United States
- Christopher Winkler Analytical Instrumentation Facility, North Carolina State University, Raleigh, North Carolina 27695, United States; © orcid.org/0000-0002-5874-0787
- Lew Reynolds Department of Materials Science and Engineering, North Carolina State University, Raleigh, North Carolina 27695, United States

Complete contact information is available at: https://pubs.acs.org/10.1021/acsanm.2c03644

Notes

The authors declare no competing financial interest.

ACKNOWLEDGMENTS

This material is based upon work supported by the National Science Foundation under grant no. 1832117. This work was also partly funded through the U.S. Army grant number

W911NF-19-1-0002 under the DoD HBCU/MI program and monitored by Air Fore Office of Scientific Research. We also thank Dr. Joe Campbell (UVA) and Dr. Charles Reyner (AFRL) for helpful discussions and valuable input. This work was performed in whole/part at the Joint School of Nanoscience and Nanoengineering, a member of the National Nanotechnology Coordinated Infrastructure (NNCI), which is supported by the National Science Foundation (grant ECCS-2025462).

REFERENCES

- (1) Senanayake, P.; Hung, C. H.; Farrell, A.; Ramirez, D. A.; Shapiro, J.; Li, C. K.; Wu, Y. R.; Hayat, M. M.; Huffaker, D. L. Thin 3D multiplication regions in plasmonically enhanced nanopillar avalanche detectors. *Nano Lett.* **2012**, *12*, 6448–6452.
- (2) Farrell, A. C.; Meng, X.; Ren, D.; Kim, H.; Senanayake, P.; Hsieh, N. Y.; Rong, Z.; Chang, T. Y.; Azizur-Rahman, K. M.; Huffaker, D. L. InGaAs—GaAs nanowire avalanche photodiodes toward single-photon detection in free-running mode. *Nano Lett.* **2018**, *19*, 582—590.
- (3) Gramsch, E. Noise characteristics of avalanche photodiode arrays of the bevel-edge type. *IEEE Trans. Electron Devices* **1998**, *45*, 1587–1594.
- (4) Zhang, J.; Itzler, M. A.; Zbinden, H.; Pan, J. W. Advances in InGaAs/InP single-photon detector systems for quantum communication. *Light: Sci. Appl.* **2015**, *4*, No. e286.
- (5) Llosá, G. Recent developments in photodetection for medical applications. *Nucl. Instrum. Methods Phys. Res., Sect. A* **2015**, 787, 353–357.
- (6) Bretz, T., Anderhub, H., Backes, M., Biland, A., Boccone, V., Braun, I., Buß, J., Cadoux, F., Commichau, V., Djambazov, L., Dorner, D. FACT-The G-APD revolution in Cherenkov astronomy. In *IEEE Nuclear Science Symposium and Medical Imaging Conference* (2013 NSS/MIC), 2013; pp. 1-8); IEEE.
- (7) Bowers, J. E., Dai, D., Kang, Y., Morse, M. High-gain high-sensitivity resonant Ge/Si APD photodetectors, 2010, May. In *Infrared Technology and Applications* XXXVI; . SPIE, (Vol. 7660; pp. 1093-1100.
- (8) Liang, Y.; Perumal Veeramalai, C. P.; Lin, G.; Su, X.; Zhang, X.; Feng, S.; Xu, Y.; Li, C. A review on III–V compound semiconductor short wave infrared avalanche photodiodes. *Nanotechnology* **2022**, *33*, 222003.
- (9) Chen, B.; Wan, Y.; Xie, Z.; Huang, J.; Zhang, N.; Shang, C.; Norman, J.; Li, Q.; Tong, Y.; Lau, K. M.; Gossard, A. C.; Bowers, J. E. Low dark current high gain InAs quantum dot avalanche photodiodes monolithically grown on Si. *ACS Photonics* **2020**, *7*, 528–533.
- (10) Hadfield, R. H. Single-photon detectors for optical quantum information applications. *Nature photonics* **2009**, *3*, 696–705.
- (11) Tosi, A.; Calandri, N.; Sanzaro, M.; Acerbi, F. Low-noise, low-jitter, high detection efficiency InGaAs/InP single-photon avalanche diode. *IEEE J. Sel. Top. Quantum Electron.* **2014**, 20, 192–197.
- (12) Zhang, J.; Itzler, M. A.; Zbinden, H.; Pan, J. W. Advances in InGaAs/InP single-photon detector systems for quantum communication. *Light: Sci. Appl.* **2015**, *4*, No. e286.
- (13) Tarof, L. E.; Knight, D. G.; Fox, K. E.; Miner, C. J.; Puetz, N.; Kim, H. B. Planar InP/InGaAs avalanche photodetectors with partial charge sheet in device periphery. *Appl. Phys. Lett.* **1990**, *57*, 670–672. (14) Shim, J.; Kang, D. H.; Yoo, G.; Hong, S. T.; Jung, W. S.; Kuh, B. J.;

Lee, B.; Shin, D.; Ha, K.; Kim, G. S.; Yu, H. Y.; Baek, J.; Park, J.-H. Germanium pin avalanche photodetector fabricated by point defect healing process. *Opt. Lett.* **2014**, *39*, 4204–4207.

(15) Virot, L.; Crozat, P.; Fédéli, J. M.; Hartmann, J. M.; Marris-

- Morini, D.; Cassan, E.; Boeuf, F.; Vivien, L. Germanium avalanche receiver for low power interconnects. *Nat. Commun.* **2014**, *5*, 4957. (16) Jain, V.; Heurlin, M.; Barrigon, E.; Bosco, L.; Nowzari, A.; Shroff,
- (16) Jain, V.; Heurlin, M.; Barrigon, E.; Bosco, L.; Nowzari, A.; Shroff, S.; Boix, V.; Karimi, M.; Jam, R. J.; Berg, A.; Samuelson, L.; Borgström, M. T.; Capasso, F.; Pettersson, H. InP/InAsP nanowire-based spatially separate absorption and multiplication avalanche photodetectors. *ACS Photonics* **2017**, *4*, 2693–2698.
- (17) Mnaymneh, K.; Dalacu, D.; McKee, J.; Lapointe, J.; Haffouz, S.; Weber, J. F.; Northeast, D. B.; Poole, P. J.; Aers, G.C.; Williams, R. L.

- On-Chip Integration of Single Photon Sources via Evanescent Coupling of Tapered Nanowires to SiN Waveguides. *Adv. Quantum Technol.* **2020**, *3*, 1900021.
- (18) Thompson, M. G.; Politi, A.; Matthews, J. C.; O'Brien, J. L. Integrated waveguide circuits for optical quantum computing. *IET circuits, devices & systems* **2011**, *5*, 94–102.
- (19) Yan, R.; Gargas, D.; Yang, P. Nanowire photonics. *Nature photonics* **2009**, 3, 569–576.
- (20) Yang, C.; Barrelet, C. J.; Capasso, F.; Lieber, C. M. Single p-type/intrinsic/n-type silicon nanowires as nanoscale avalanche photodetectors. *Nano Lett.* **2006**, *6*, 2929–2934.
- (21) Reimer, M. E.; Van Kouwen, M. P.; Barkelid, M.; Hocevar, M.; Van Weert, M. H.; Algra, R. E.; Bakkers, E. P.; Björk, M. T.; Schmid, H.; Riel, H.; Kouwenhoven, L. P. Single photon emission and detection at the nanoscale utilizing semiconductor nanowires. *J. Nanophotonics* **2011**, *5*, 053502.
- (22) Yang, K.; Kwak, K.; Kim, S. Influence of the intrinsic length on p +-i-n+ Si nanowire avalanche photodetectors on flexible plastic substrates. *Phys. Status Solidi C* **2014**, *11*, 217–221.
- (23) Bulgarini, G.; Reimer, M. E.; Hocevar, M.; Bakkers, E. P.; Kouwenhoven, L. P.; Zwiller, V. Avalanche amplification of a single exciton in a semiconductor nanowire. *Nat. Photonics* **2012**, *6*, 455–458.
- (24) Chuang, L. C.; Sedgwick, F. G.; Chen, R.; Ko, W. S.; Moewe, M.; Ng, K. W.; Tran, T. T. D.; Chang-Hasnain, C. GaAs-based nanoneedle light emitting diode and avalanche photodiode monolithically integrated on a silicon substrate. *Nano Lett.* **2011**, *11*, 385–390.
- (25) Hayden, O.; Agarwal, R.; Lieber, C. M. Nanoscale avalanche photodiodes for highly sensitive and spatially resolved photon detection. *Nat. Mater.* **2006**, *5*, 352–356.
- (26) Gibson, S. J.; van Kasteren, B.; Tekcan, B.; Cui, Y.; van Dam, D.; Haverkort, J. E.; Bakkers, E. P.; Reimer, M. E. Tapered InP nanowire arrays for efficient broadband high-speed single-photon detection. *Nat. Nanotechnol.* **2019**, *14*, 473–479.
- (27) Parakh, M.; Pokharel, R.; Dawkins, K.; Devkota, S.; Li, J.; Iyer, S. Ensemble GaAsSb/GaAs axial configured nanowire-based separate absorption, charge, and multiplication avalanche near-infrared photodetectors. *Nanoscale Adv.* **2022**, *4*, 3919–3927.
- (28) Anabestani, H.; Shazzad, R.; Fattah, M. F.; Therrien, J.; Ban, D. Review on GaAsSb nanowire potentials for future 1D heterostructures: Properties and applications. *Mater. Today Commun.* **2021**, 28, 102542.
- (29) Kim, Y.; Joyce, H. J.; Gao, Q.; Tan, H. H.; Jagadish, C.; Paladugu, M.; Zou, J.; Suvorova, A. A. Influence of nanowire density on the shape and optical properties of ternary InGaAs nanowires. *Nano Lett.* **2006**, *6*, 599–604.
- (30) Dheeraj, D. L.; Patriarche, G.; Largeau, L.; Zhou, H. L.; van Helvoort, A. T. J.; Glas, F.; Harmand, J. C.; Fimland, B. O.; Weman, H. Zinc blende GaAsSb nanowires grown by molecular beam epitaxy. *Nanotechnology* **2008**, *19*, 275605.
- (31) Ren, D.; Ahtapodov, L.; Nilsen, J. S.; Yang, J.; Gustafsson, A.; Huh, J.; Conibeer, G. J.; van Helvoort, A. T.; Fimland, B. O.; Weman, H. Single-mode near-infrared lasing in a GaAsSb-based nanowire superlattice at room temperature. *Nano Lett.* **2018**, *18*, 2304–2310.
- (32) Yang, I.; Zhang, X.; Zheng, C.; Gao, Q.; Li, Z.; Li, L.; Lockrey, M. N.; Nguyen, H.; Caroff, P.; Etheridge, J.; Tan, H. H.; Jagadish, C.; Wong-Leung, J.; Fu, L. Radial growth evolution of InGaAs/InP multiquantum-well nanowires grown by selective-area metal organic vaporphase epitaxy. *ACS Nano* **2018**, *12*, 10374–10382.
- (33) Shin, J. C.; Kim, K. H.; Yu, K. J.; Hu, H.; Yin, L.; Ning, C. Z.; Rogers, J. A.; Zuo, J. M.; Li, X. In x Ga1-x As nanowires on silicon: One-dimensional heterogeneous epitaxy, bandgap engineering, and photovoltaics. *Nano Lett.* **2011**, *11*, 4831–4838.
- (34) Royo, M.; De Luca, M.; Rurali, R.; Zardo, I. A review on III–V core–multishell nanowires: growth, properties, and applications. *J. Phys. D: Appl. Phys.* **2017**, *50*, 143001.
- (35) Ren, D.; Huh, J.; Dheeraj, D. L.; Weman, H.; Fimland, B. O. Influence of pitch on the morphology and luminescence properties of self-catalyzed GaAsSb nanowire arrays. *Appl. Phys. Lett.* **2016**, *109*, 243102.

- (36) Hall, K. C.; Leonard, S. W.; van Driel, H. M.; Kost, A. R.; Selvig, E.; Chow, D. H. Subpicosecond spin relaxation in GaAsSb multiple quantum wells. *Appl. Phys. Lett.* **1999**, *75*, 3665–3667.
- (37) Chiu, Y. S.; Ya, M. H.; Su, W. S.; Chen, Y. F. Properties of photoluminescence in type-II GaAsSb/GaAs multiple quantum wells. *J. Appl. Phys.* **2002**, *92*, 5810–5813.
- (38) Kasanaboina, P. K.; Ojha, S. K.; Sami, S. U.; Reynolds, C. L.; Liu, Y.; Iyer, S. Bandgap tuning of GaAs/GaAsSb core-shell nanowires grown by molecular beam epitaxy. *Semicond. Sci. Technol.* **2015**, *30*, 105036.
- (39) Kasanaboina, P. K.; Ojha, S. K.; Sami, S. U.; Reynolds, L., Jr.; Liu, Y.; Iyer, S.; SPIE, 2015, February; Vol. 9373, pp 30–38. Tailoring of GaAs/GaAsSb core-shell structured nanowires for IR photodetector applications Quantum Dots and Nanostructures: Synthesis, Characterization, and Modeling XII DOI: 10.1117/12.2080572
- (40) Saleh, M. A.; Hayat, M. M.; Sotirelis, P. P.; Holmes, A. L.; Campbell, J. C.; Saleh, B. E.; Teich, M. C. Impact-ionization and noise characteristics of thin III-V avalanche photodiodes. *IEEE Trans. Electron Devices* **2001**, 48, 2722–2731.
- (41) Ramaswamy, P.; Devkota, S.; Pokharel, R.; Nalamati, S.; Stevie, F.; Jones, K.; Reynolds, L.; Iyer, S. A study of dopant incorporation in Te-doped GaAsSb nanowires using a combination of XPS/UPS, and C-AFM/SKPM. *Sci. Rep.* **2021**, *11*, 8329.
- (42) Ramaswamy, P.; Pokharel, R.; Parakh, M.; Jones, K.; Li, J.; Iyer, S. Be-doping assessment in Self-Catalyzed MBE Grown GaAs Nanowires. In CLEO: Science and Innovations; Optica Publishing Group, 2021, May, p SW2F-7.
- (43) Devkota, S.; Parakh, M.; Johnson, S.; Ramaswamy, P.; Lowe, M.; Penn, A.; Reynolds, L.; Iyer, S. A study of n-doping in self-catalyzed GaAsSb nanowires using GaTe dopant source and ensemble nanowire near-infrared photodetector. *Nanotechnology* **2020**, *31*, 505203.
- (44) Zhu, X.; Lin, F.; Zhang, Z.; Chen, X.; Huang, H.; Wang, D.; Tang, J.; Fang, X.; Fang, D.; Ho, J. C.; Liao, L.; Wei, Z. Enhancing performance of a GaAs/AlGaAs/GaAs nanowire photodetector based on the two-dimensional electron—hole tube structure. *Nano Lett.* **2020**, 20, 2654–2659.
- (45) Farrell, A. C.; Senanayake, P.; Hung, C. H.; El-Howayek, G.; Rajagopal, A.; Currie, M.; Hayat, M. M.; Huffaker, D. L. Plasmonic field confinement for separate absorption-multiplication in InGaAs nanopillar avalanche photodiodes. *Sci. Rep.* **2015**, *5*, 1–6.
- (46) Pokharel, R.; Ramaswamy, P.; Devkota, S.; Parakh, M.; Dawkins, K.; Penn, A.; Cabral, M.; Reynolds, L.; Iyer, S. Epitaxial high-yield intrinsic and Te-doped dilute nitride GaAsSbN nanowire heterostructure and ensemble photodetector application. *ACS Appl. Electron. Mater.* **2020**, *2*, 2730–2738.
- (47) Groves, C.; Ghin, R.; David, J. P. R.; Rees, G. J. Temperature dependence of impact ionization in GaAs. *IEEE Trans. Electron Devices* **2003**, *50*, 2027–2031.
- (48) Parakh, M.; Devkota, S.; Pokharel, R.; Dawkins, K.; Kuchoor, H.; Li, J.; Iyer, S. Heterostructure axial GaAsSb ensemble near-infrared p-in based axial configured nanowire photodetectors. *Nanotechnology* **2023**, *4*, 3919–3927.
- (49) Sharma, M.; Karim, M. R.; Kasanaboina, P.; Li, J.; Iyer, S. Pitch-Induced bandgap tuning in self-catalyzed growth of patterned GaAsSb axial and GaAs/GaAsSb core—shell nanowires using molecular beam epitaxy. *Cryst. Growth Des.* **2017**, *17*, 730—737.
- (50) Deshmukh, P.; Sharma, M.; Nalamati, S.; Reynolds, C. L.; Liu, Y.; Iyer, S. Molecular beam epitaxial growth of high quality Ga-catalyzed GaAs1–xSbx (x> 0.8) nanowires on Si (111) with photoluminescence emission reaching 1.7 μ m. Semicond. Sci. Technol. 2018, 33, 125007.
- (51) Kaspi, R.; Evans, K. R. Sb-surface segregation and the control of compositional abruptness at the GaAsSbGaAs interface. *J. Cryst. Growth* **1997**, *175-176*, 838–843.
- (52) Hayat, M. M.; Saleh, B. E.; Teich, M. C. Effect of dead space on gain and noise of double-carrier-multiplication avalanche photodiodes. *IEEE Trans. Electron Devices* **1992**, *39*, 546–552.
- (53) Rudolph, D.; Schweickert, L.; Morkötter, S.; Loitsch, B.; Hertenberger, S.; Becker, J.; Bichler, M.; Abstreiter, G.; Finley, J. J.; Koblmüller, G. Effect of interwire separation on growth kinetics and

properties of site-selective GaAs nanowires. *Appl. Phys. Lett.* **2014**, *105*, 033111.

- (54) Berg, A.; Caroff, P.; Shahid, N.; Lockrey, M. N.; Yuan, X.; Borgström, M. T.; Tan, H. H.; Jagadish, C. Growth and optical properties of In x Ga 1– x P nanowires synthesized by selective-area epitaxy. *Nano Res.* **2017**, *10*, 672–682.
- (55) Sonner, M. M.; Sitek, A.; Janker, L.; Rudolph, D.; Ruhstorfer, D.; Döblinger, M.; Manolescu, A.; Abstreiter, G.; Finley, J. J.; Wixforth, A.; Koblmüller, G.; Krenner, H. J. Breakdown of corner states and carrier localization by monolayer fluctuations in radial nanowire quantum wells. *Nano Lett.* **2019**, *19*, 3336–3343.
- (56) Nouri, M.; Ghadimi, A. Reduction of dark current and gain increase in InAs avalanche photodiode with AlGaAs blocking layer. *Optik* **2017**, *148*, 268–274.
- (57) Woodson, M. E.; Ren, M.; Maddox, S. J.; Chen, Y.; Bank, S. R.; Campbell, J. C. Low-noise AlInAsSb avalanche photodiode. *Appl. Phys. Lett.* **2016**, *108*, 081102.

□ Recommended by ACS

Non-Uniformly Strained Core-Shell InAs/InP Nanowires for Mid-Infrared Photonic Applications

Vladimir Fedorov, Ivan Mukhin, et al.

MARCH 16, 2023

ACS APPLIED NANO MATERIALS

READ 🗹

Gallium Phosphide Nanowires Grown on SiO₂ by Gas-Source Molecular Beam Epitaxy

Songdan Kang, Fariba Hatami, et al.

MARCH 10, 2023

CRYSTAL GROWTH & DESIGN

READ 🗹

AlGaN UV Detector with Largely Enhanced Heat Dissipation on Mo Substrate Enabled by van der Waals Epitaxy

Yang Chen, Dabing Li, et al.

DECEMBER 23, 2022

CRYSTAL GROWTH & DESIGN

READ 🗹

Laser Scribing for Electrode Patterning of Perovskite Spectrometer-Grade CsPbBr₃ Gamma-ray Detectors

Vladislav V. Klepov, Mercouri G. Kanatzidis, et al.

MARCH 24, 2023

ACS APPLIED MATERIALS & INTERFACES

READ 🗹

Get More Suggestions >